Open Archive TOULOUSE Archive Ouverte (OATAO)

This is an author's version published in : http://oatao.univ-toulouse.fr/19954

Official URL : https://dx.doi.org/10.1016/j.ijhydene.2017.01.184

Coupled continuum and condensation— evaporation pore network model of the cathode in polymer-electrolyte fuel cell

Najib Belgacem [a,b,c], Marc Prat [a,b,**], Joel Pauchet [c,*]

[a] INPT, UPS, IMFT (Institut de Mécanique des Fluides de Toulouse), Université de Toulouse, Allée Camille Soula, F-31400 Toulouse, France
[b] CNRS, IMFT, F-31400 Toulouse, France
[c] Univ. Grenoble Alpes, CEA LITEN, DEHT, 17 Rue Martyrs, F-38054 Grenoble, France

ARTICLE INFO

ABSTRACT

A model of the cathode side of a Proton Exchange Membrane Fuel Cell coupling the transfers in the GDL with the phenomena taking place in the cathode catalyst layer and the protonic transport in the membrane is presented. This model combines the efficiency of pore network models to simulate the liquid water formation in the fibrous substrate of the gas diffusion layer (GDL) and the simplicity of a continuum approach in the micro-porous layer (MPL). The model allows simulating the liquid pattern inside the cathode GDL taking into account condensation and evaporation phenomena under the assumption that the water produced by the electro-chemical reactions enters the MPL in vapor form from the catalyst layer. Results show the importance of the coupling between the transfers within the various layers, especially when liquid water forms as the result of condensation in the region of the GDL fibrous substrate located below the rib.

Introduction

Proton Exchange Membrane Fuel Cell (PEMFC) is considered as a key alternative to thermal engines for transport application, allowing no use of oil fuels and no emission of greenhouse gases. Numerous studies have been conducted in the last thirty years to increase its performance and durability, and reduce its cost, which are the three main bottlenecks to be solved to ensure the mass market development of this solution. Water management remains up-to-date a major limiting factor to performance and durability of PEMFC, see for instance Ref. [1]. Inside the Membrane Electrode Assembly (MEA) a trade-off is to be found between drying and flooding. Drying occurs when the membrane and/or the ionomer in the active layers do not contain enough water to ensure good proton conductivity, whereas flooding occurs when too much

liquid water is present inside the MEA and reduces the gas access to the catalytic sites. In addition to increasing the performance, a controlled water management also allows increasing the durability of PEMFC as some degradation mechanisms are linked to the presence of liquid water and/or to the level of water vapor partial pressure inside the catalyst layer, see for instance Ref. [2].

Water management is closely linked to the operating conditions of the PEMFC (temperature, pressure and hydration of the gases, steady-state or transient…) but also to the properties of the layers used in the MEA, gas diffusion layer, catalyst layer and membrane. The multiple and conflicting functions of these layers (electrical and thermal conduction, gas diffusion and liquid water removal) and their coupling, see for instance Ref. [3], make however complex their optimization by semi-empirical trial and error test procedures. The development of more descriptive and predictive numerical simulation tools is necessary to better understand water management inside the MEA and its link to the properties of the layers. This is mandatory to progress towards "design" tools.

Important developments have been carried out in this domain for several years, such as the modeling of the MEA with more and more sophisticated representations of the various layers, see for instance Ref. [4], or the progressive consideration of the coupling between electrical, fluidic and thermal transports [5]. In these models, see also Ref. [6], the two-phase transport is based on the classical continuum approach to porous media. These models have allowed making progress in the understanding of the transfers within the PEMFC. However, the relevance of this approach has been questioned, i.e. Ref. [7], because of the capillary regime prevailing in the gas diffusion layers (GDL) and the obvious lack of length scale separation (only a few pores over the thickness of the fibrous substrate of the GDL). The latter is generally a two-layer system resulting from the assembly of a fibrous substrate, referred to as the diffusion medium (DM), and a micro-porous layer (MPL).

As an alternative, Pore Network Model (PNM) has been applied to PEMFC. PNM is well adapted to model the capillary regime, especially in thin layers such as the DM of the GDL, e.g. Ref. [8], as well as the more complex cases where the wettability is mixed (mixed refers here to situations where hydrophilic pores and hydrophobic pores coexist in the DM), e.g. Refs. [9,10]. For this reason, the use of PNM has up-to-date mainly focused on the DM even if some developments have also been conducted for the Cathode Catalyst Layer (CCL), e.g. Ref. [11]. To our knowledge, PNM has not been applied to the micro-porous layer (MPL) of the GDL, at least as a tool of simulation directly at the scale of the pore network of a MPL. However, results obtained from PNM simulations are exploited for example in Ref. [12] to study the optimal thickness of the MPL. For this reason, PNM is used in the present work to model the liquid water formation in the DM.

Regarding the simulation of two-phase flows in the DM with PNM, one can distinguish the simulations performed in conjunction with ex-situ experiments from the more challenging simulations aiming at predicting the liquid water distributions within the GDL in an operating fuel cell. Regarding the former, recent works have confirmed that a standard invasion percolation algorithm is well adapted to

describe the ex-situ situation where typically liquid water is injected from one side in a dry GDL [13,14], at least when the medium is hydrophobic.

The situation regarding the in-situ case is much less clear. In a majority of works, see references in [15], a scenario similar to the ex-situ case is considered. Namely, liquid water enters the GDL in liquid phase from the CCL. This situation of liquid water injection is referred to as the injection scenario.

However, a completely different option is considered in Ref. [15] where it is assumed that water enters the GDL in vapor form. According to the scenario considered in Ref. [15], liquid water can form in the DM as a result of the condensation of the water vapor in the colder zones of the DM (essentially in the region of the DM below the ribs). This situation of liquid water condensation is referred to as the condensation scenario. An important feature of the model in Ref. [15] is therefore to take into account the temperature variations within the GDL. The liquid distribution is significantly different between the two options. As discussed in Ref. [15], the condensation scenario is in good agreement with several experimental results presented in Refs. [16,17], noting that these experiments are performed at temperatures close to the standard operating temperature of PEMFC (~80 °C). As in the experiments [16], the simulations show that the GDL is completely dry at sufficiently low current density and/or relative humidity in the channel. As in the experiments [16], a strong rib–channel separation effect is observed when liquid water is present, i.e. the liquid water accumulates in the region below the rib and no water is observed bellow the channels. As in the experiments [17], the saturation along the DM thickness increases from CCL to rib/channel area, whereas this saturation typically decreases according to the simulations based on the liquid injection scenario, e. g. Ref. [18]. The impact of average current density and channel relative humidity on saturation profiles are also consistent with the experimental results reported in Ref. [17]. Despite all these elements showing several points of good agreement between the experiments and the simulations, we do not claim that the PNM presented in Ref. [15], is adapted to describe all the situations encountered in PEMFC as regards the liquid water formation and displacement in the GDL. For instance, it could be not sufficient when the operating temperature is significantly colder than 80 °C or when the relative humidity in the channel is close to 100%. Further work is needed to test or improve the model for those conditions. Nevertheless, based on the overall good agreement between the condensation–evaporation PNM [15,19] and several experimental observations as mentioned above, the model presented in what follows adopts the same option as in Ref. [15] as regards the computation of the liquid water formation.

It can be noted that the consideration of condensation phenomenon in a discrete approach as a key aspect of liquid water in the DM is not restricted to the works presented in Refs. [15,19]. A condensation algorithm is also presented in Refs. [20,21] and the conclusion is that condensation has a significant influence of the liquid distribution. However, the model is different from the one proposed in Ref. [15]. This is actually not a PNM but a somewhat different discrete approach. In contrast with the model presented in Ref. [15], only simulations in 2D discrete structures are presented in

Refs. [20,21], and liquid injection is considered together with condensation. Thus, the fact that the GDL can be completely dry is not pointed out. The condensation algorithm is completely different and relies on a coupling with a continuum model to compute the source—sink terms in the GDL associated with condensation and evaporation phenomena. By contrast, all the phenomena are directly computed at the pore network scale in the DM (which is referred to as the fibrous substrate (FS) in Refs. [20,21]), in our model. We can also mention the recent numerical work presented in Ref. [22] on the impact of the MPL. This work is based on a two-dimensional dynamic pore network taking into account the condensation evaporation phenomena. There is, however, no coupling with the electrochemical phenomena in the CCL.

Compared to the model presented in Ref. [15], the objective of the present article is to improve the modeling of the cathode by essentially coupling the PNM presented in Ref. [15] with the phenomena occurring in the adjacent layers, namely the MPL, CCL and the membrane and in particular with the electrochemical reactions taking place in the CCL.

In Ref. [15], only the DM is considered and important data such as the current density and heat flux distributions at the DM inlet are not computed but are imposed as input data. By introducing the coupling, these data will be outputs of the computations. Another important objective is to evaluate the impact of the coupling on the results obtained using the simpler approach proposed in Ref. [15]. As we shall see the coupling is performed by coupling the PNM describing the transport phenomena and the water formation in the DM, with continuum models for the MPL, and with the phenomena taking place in the CCL.

Developing mixed approaches coupling PNM and continuum models is not a novelty in the context of PEMFC. The previously mentioned work presented in Ref. [21] is an example. More recently, on can refer to the works presented in Ref. [23], where three different coupling methods are discussed. The pore network is however only 2D and again it is assumed that water enters in liquid form into the GDL. As a result the liquid distribution in the DM depicted in this paper (see Fig. 10 in Ref. [23]) has nothing to do with the liquid distributions presented in Ref. [15]. This also holds for the liquid water distributions computed by the same group in Ref. [24]. Interestingly, the temperature in Ref. [24] is quite low (25 °C), much below the standard operating temperature (~80 °C) considered in Ref. [15]. A coupled continuum-PN models is also presented in Ref. [25]. This model couples a three-dimensional PNM in the GDL to continuous models in the other layers for anode and cathode sides. However, this model is limited to isothermal situations and the injection scenario in the DM (no MPL is modeled) for which the injection points at the interface GDL/CCL are inputs of the models. The condensation phenomenon is completely ignored.

The paper is organized as follows. The fuel cell cathode sub-domain of interest is described in Section "Cathode unit cell". The physical models used in the different layers are presented in Section "Transport phenomena in GDL and associated boundary conditions (dry condition)". The pore network approach for computing the various transport phenomena in the DM is presented in Section "Pore network approach of transport in DM". Section "Continuum approach of transport in MPL" describes the continuum model used for the MPL. The CCL and membrane discrete representations are presented in Section "Catalyst Layer and membrane". The coupling procedure is described in Section "Coupling GDL with CCL and membrane". Results are presented and discussed in Section "Results and discussion". Finally conclusions are discussed in Section "Conclusions".

Cathode unit cell

As depicted in Fig. 1, our model is developed at the rib/channel scale, which means over a domain adjacent to one rib and two half-channels. The corresponding domain is referred to as a cathode unit cell. The domain includes the GDL (DM and MPL), the cathode catalyst layer (CCL) and the membrane. As we shall see transport equations are discretized over the GDL (MPL + DM) only, whereas computational cells located in the membrane and the (CCL) are used in the coupling procedure.

The domain is 3D with extension into the y direction (flow direction in the channel). It can be noted that this feature is not useful when only single phase transports are considered in the cathode as the boundary conditions applied along y are uniform. Nevertheless, even with uniform boundary conditions in y direction, this 3D extension is mandatory when liquid water is considered as connectivity properties of the liquid and gas phase at the pore network scale are different in 3D and in 2D [26].

The compressibility of the GDL is taken into account in our model as it has an influence on transfers below the rib and below the channel. As indicated in Fig. 1, the thickness of the uncompressed GDL is 240 μm corresponding to the sum of the DM (190 μm) and of the MPL (50 μm), as for the SGL 25BC used as a reference GDL for this study (see SGL web site). The CCL has a thickness of 6 μm (typical of catalyst loading around 0.4 mgPt/cm^2) and the membrane is 12.5 μm in thickness (typical of Nafion NR-211). The compression of the GDL below the rib (due to the clamping pressure) is set at 20% of the uncompressed DM (so 38 μm), as classically used in performance tests.

The unit cell is considered as the representative cell of a spatially periodic system. As a result, spatially periodic boundary conditions are applied on the lateral, front and back surfaces of the unit cell for each considered transport phenomenon (heat, electrical current, liquid water, vapor water,
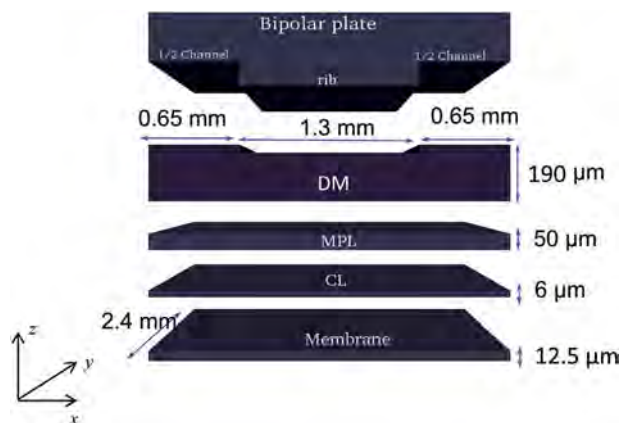

Fig. 1 — Cathode model at the rib—channel scale.

and O_2). These boundary conditions are thus not discussed anymore in what follows where the focus is on the more important boundary conditions along the GDL/rib-channel interface and along the MPL/CCL interface.

Transport phenomena in GDL and associated boundary conditions (dry condition)

Gas transport

As discussed in Ref. [15] and mentioned in the introduction, an important feature directly related to the assumption of the water entering in vapor phase into the GDL is that the GDL can be dry without any liquid water formation when the current density and/or the relative humidity in the channel are sufficiently low. For this reason, the case of the dry GDL is distinguished from the case of the wet GDL.

For the dry condition only gas (water vapor, nitrogen and oxygen) is present in the GDL. The various transport mechanisms considered are summarized in Fig. 2. Gas, thermal and electrical transfers are considered in the GDL (DM and MPL) under the following assumptions: i) nitrogen is a stagnant gas, ii) water vapor and oxygen diffuse in the pore space according to Fick's law. Assuming for the moment that the DM and MPL can be described as effective media (continuum approach), the diffusion problem is thus expressed as

$$J_{H_2O} = -\mathbf{D}_{H2O} \cdot \nabla c_{H_2O} \tag{1}$$

$$J_{O_2} = -\mathbf{D}_{O2} \cdot \nabla c_{O_2} \tag{2}$$

where J_{H2O}, J_{O2} are the molar fluxes (mol m^{-2} s^{-1}), c_{H_2O} and c_{O_2} are the molar concentrations (mol m^{-3}), and $\mathbf{D}_{H2O}$ and $\mathbf{D}_{O2}$ are the effective diffusion tensor of water vapor and oxygen respectively. The mass conservation of each species is expressed as,

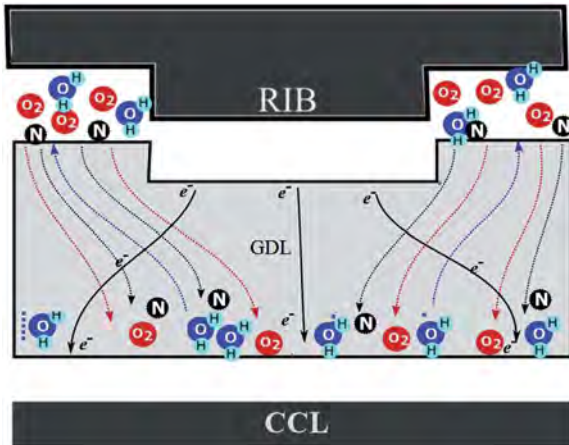$$\nabla \cdot J_{H_2O} = 0. \tag{3}$$

$$\nabla \cdot J_{O_2} = 0. \tag{4}$$

The above equations are solved using the following boundary conditions, summarized in Fig. 3. Assuming ideal gas behavior in the channel, the gas concentrations is imposed at the GDL/gas channel interface as a function of relative humidity (RH), oxygen partial pressure (P_{O2}), nitrogen partial pressure (P_{N2}), gas temperature (T), and total pressure (P_{tot}) of gases in the channel,

$$c_{H_2O} = \frac{P_{H_2O}}{RT} \tag{5}$$

$$c_{O_2} = \frac{P_{O_2}}{RT} \tag{6}$$

where

$$P_{tot} = P_{H_2O} + P_{O_2} + P_{N_2} \tag{7}$$

$$P_{H_2O} = x_{H_2O} P_{tot} = RH \, P_{sat} \tag{8}$$

$$P_{O_2} = x_{O_2} P_{tot} \tag{9}$$

$$P_{sat} = exp\left(23.1961 - \frac{3816.44}{T - 46.13}\right) \tag{10}$$

where x_i is the mole fraction of species i.

Zero flux of vapor water and oxygen is imposed at the GDL/rib interface.

At the GDL/CCL interface, it is assumed that only a fraction of the water flux j_{H_2OCCL} produced by the electrochemical reactions in the CCL is transferred through the GDL (the complementary fraction is transferred through the membrane on the anode side). Thus, we impose on this interface,

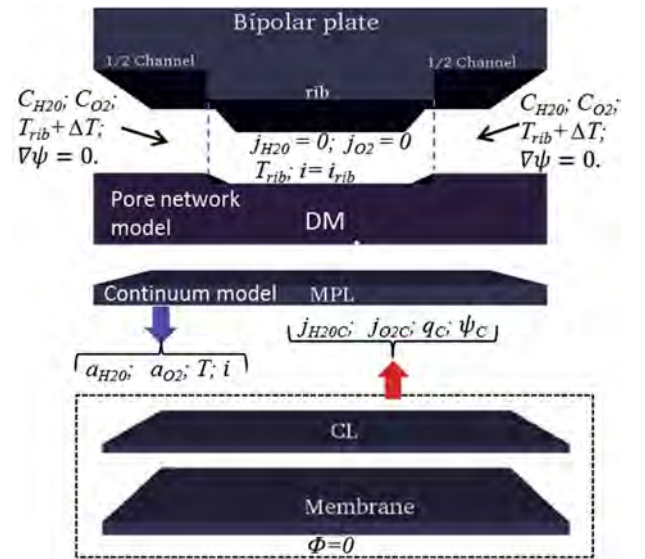$$j_{netH_2O, c} = \gamma_m j_{H_2OC} \tag{11}$$

Fig. 3 – Summary of boundary conditions applied for the computations of transport phenomena in GDL. Spatially periodic boundary conditions are imposed on lateral sides of domain.

Fig. 2 – Transfer mechanisms considered in the cathode GDL for the dry condition.

where the partition coefficient γ_m is typically in the range 0.5 −0.8 according to unpublished measurements performed at CEA/LITEN (LITEN is the laboratory to which one of the paper co-authors belongs). How j_{H_2OC} is computed is explained below (see Eq. (26)). As mentioned in the introduction, it is assumed that the flux given by Eq. (11) is a water vapor flux (and not a liquid flux).

Similarly a flux condition is imposed at the GDL/CCL interface as regards the oxygen transport problem assuming no permeation through the membrane,

$$j_{O_2, c} = j_{O_2C} \qquad (12)$$

How j_{O_2C} is computed is explained below (see Eq. (25)).

Heat transfer

The heat transfer is modeled according to Fourier's law

$$q = -\kappa \cdot \nabla T \qquad (13)$$

$$\nabla \cdot q = 0. \qquad (14)$$

where q, T, and κ are the heat flux (W m^{-2}), temperature (K), and thermal conductivity tensor (W m^{-1} K^{-1}) of the GDL respectively.

The boundary conditions are the following. The rib temperature is known. Thus $T = T_{rib}$ is imposed at this interface. The temperature is also imposed at the channel/GDL interface with $T_{channel} = T_{rib} + \Delta T$ where ΔT is an input data. Typically $\Delta T = 2$−5 °C according to unpublished measurements performed at CEA/LITEN. The heat flux is imposed at the GDL/CCL interface. Similarly as for the water flux it is assumed that only a fraction of the heat flux generated in the CCL is transferred through the cathode GDL,

$$q_{net,c} = \gamma_q q_C \qquad (15)$$

where the partition factor γ_q is also typically in the range 0.5 −0.8 according to unpublished measurements performed at LITEN. How q_C is computed is explained below (see Eq. (27)).

Electrical transport

The electron transport is computed thanks to Ohm's law

$$i = -\sigma \cdot \nabla \psi \qquad (16)$$

$$\nabla \cdot i = 0 \qquad (17)$$

where i, σ, and ψ are the current density (A m^{-2}), electrical conductivity tensor (S m^{-1}), and electronic potential (V) respectively.

Zero flux on electrical potential (current density is zero) is imposed at the GDL/channel interface whereas the current density i_{rib} is imposed at the GDL/rib interface so that the current density $i_{rib} S_{rib} = I$ where I is the total current (Amps) measured at cell level (S_{rib} is the surface area of the rib). The electrical potential ψ is imposed at the GDL/CCL interface,

$$\psi = \psi_C \qquad (18)$$

How ψ_C is computed is explained below (see Eq. (36)).

Due to its fibrous structure, the DM is considered as an anisotropic and deformable medium. The MPL is isotropic and not deformable owing to its granular structure. Accordingly, the transport tensors above are supposed isotropic for the MPL and identical in the regions below the rib and below the channel, whereas for the DM, the coefficients of the tensors are different in the in-plane and through-plane directions as well as below the rib and the channel. Details are given in the Appendix.

When the conditions are such that liquid water forms inside the GDL, the GDL is said to be wet. The presence of the liquid water has an impact on the transport. How this impact is taken into account in the model is described in Section "Pore network approach of transport in DM".

As explained below, the steady-state solution obtained when liquid water forms inside the GDL corresponds to a situation where a balance is reached between the condensation rate and the evaporation rate at the boundary of each liquid clusters present in the DM. It turns out that liquid water never reaches the channel in the cases we considered. Therefore the formulation of the boundary condition at the GDL/channel interface is the same for a dry GDL and a wet GDL. As reported in previous studies, e.g. Ref. [27], more involved situations with droplet formation at the channel/ GDL interface exist but the corresponding situations (colder operating temperature, higher relative humidity in the channel) are beyond the scope of the present model. Zero flux of liquid is imposed at the rib/GDL interface.

Pore network approach of transport in DM

For simplicity, the interface between the two layers, namely the DM and the MPL, forming the GDL is assumed to be perfectly flat. The DM pore space is modeled as a 3D cubic pore network with a lattice spacing of 50 μm, leading to 52 pores in the rib/channel length, 5 in the thickness, and 52 in the direction of the channel (each pore is shown as gray cube in Fig. 4). Each pore is cubic and is connected to six throats of square cross-section.

The throat sizes d_t are randomly distributed in the range [20 μm, 34 μm] according to a Weibull's law as in Refs. [9,10],

$$d_t = d_{t_{min}} + (d_{t_{max}} - d_{t_{min}})$$
$$\times \left[\left\{ -\delta \ln\left(\lambda' \left(1 - \exp\left(-\frac{1}{\delta}\right) \right) \right) + \exp\left(-\frac{1}{\delta}\right) \right\}^{\frac{1}{\gamma}} \right] \qquad (19)$$

with δ=0.1, γ=4.7, and λ' is random number in the range [0,1].
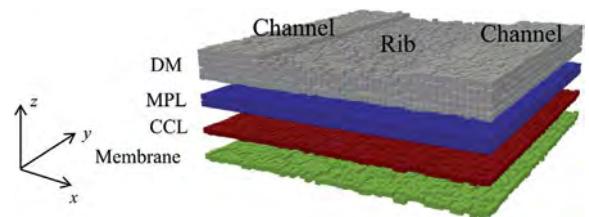
Fig. 4 − Meshing of DM, MPL, catalyst layer, and membrane.

Then the size of each of the 52*52*5 cubic pores is specified as follows. Each pore diameter is first initialized to the maximum diameter of its neighboring throats, then adjusted to fit to the porosity ($\varepsilon = 0.8$) of the DM. This adjustment is done by multiplying each pore diameter by the same factor.

In the DM, two networks are actually created: the "fluid network" for the fluid transfers (in the pore space of the DM) and the "solid network" for the electrical and thermal transfers (in the fibers, binders… of the DM). The same number N of pores is considered for the solid and fluid networks. This is not fully consistent since as sketched in Fig. 5 it is more representative to locate the solid network nodes at positions different (shifted) from the nodes of the fluid network. As sketched in Fig. 5b, collocated solid and fluid networks are actually considered in the modeling. Nevertheless, this assumption has no influence on the results since no fluid/solid interactions are considered as regards the electrical and heat transfers. Diameters of the links in the solid network are also distributed according to a Weibull's law.

The transport phenomena in the DM are thus solved using the pore network approach, e.g. Ref. [8]. Since the diffusion transport in the gas phase, the heat and electric transports in the solid are basically governed by the same type of (diffusion) equation, the network formulation of the various transports is similar.

Conservation at each network node i (surrounded by s nodes) is expressed as

$$\sum_{surrounding\ pores\ s} j_{i,\ s} = 0 \tag{20}$$

where $j_{i,s}$ is the flux into node i from surrounding pore s, $j_{i,s} = g_{i,s}\,(X_s - X_i)$ where X is the variable associated with the transfer mode considered (electrical, thermal transfers or gas diffusion).

The general formulation of the local conductance between nodes i and s is given as the harmonic average of the conductance $g_{l\ i,s}$ of the link between the two nodes, and those g_{pi} and g_{ps} of each half node:

$$\frac{1}{g_{i,s}} = \frac{1}{g_{p_i}} + \frac{1}{g_{ps}} + \frac{1}{g_{l\ i,s}} \tag{21}$$

where

$$g_p = \beta \frac{G_X S_p}{L_p} \tag{22}$$

and

$$g_l = \beta \frac{G_X S_l}{L_l} \tag{23}$$

where L_l, L_p, S_l, S_p are the local lengths L and cross-section surface areas S of the half nodes and of the link. These parameters are local and depend on the local structure of the GDL. G_X is the "conductivity" for the transfer considered (thermal and electrical conductivities, binary diffusion). It is the same everywhere within the GDL volume. β is a fitting parameter that is adjusted to experimental results. Its value is different between in-plane and through-plane so as to take into account the anisotropy of the DM and below the rib and the channel so as to take into account the effect of the clamping pressure.

For electronic transfer, $j_{i,s} = g_{i,s}\,(\psi_s - \psi_i)$, and $G_X = \sigma_e$, which is the electrical conductivity of the carbon fibers (61,000 S m^{-1}) [28,29].

For heat transfer, $j_{i,s} = g_{i,s}\,(T_s - T_i)$, and $G_X = \kappa$, which is the thermal conductivity of the carbon fibers (129 W m^{-1} K^{-1}) [28,29].

For gas diffusion, $j_{i,s} = g_{i,s}\,(C_s - C_i)$, and $G_X = D_{bin}$, which is the binary coefficient diffusion of water vapor in air: 0.260 cm^2 s^{-1} [30], or Oxygen in air: $D_{bin} = 3.2.\,10^{-5} \left(\frac{T}{353}\right)^{1.5} 1/p$ (m^2 s^{-1}) where p is the absolute pressure [20].

When liquid water is present in the DM, only the gas diffusion is modified by the presence of liquid water. According to Burheim et al. [31], it would be interesting, however, to include in the future also the influence of liquid water on thermal effective conductivity. No gas diffusion can occur in the pores/throats fully invaded by the liquid whereas the local conductance g_{liq} of the pore (and the throat) is modified as

$$g_{liq} = g\,(1 - S) \tag{24}$$

where S is the local water saturation of the pore and/or of the throat in the partially invaded throat or pore.

The values of the conductances and fitting parameters β from experimental results are given in the Appendix.

Continuum approach of transport in MPL

A direct pore network approach in the MPL implies considering a network much finer than in the DM since the pore sizes in the MPL are much smaller (typically on the order of 0.3–0.5 μm compared to 30–50 μm in the DM). For this reason and the fact that liquid water actually does not form in the MPL for the
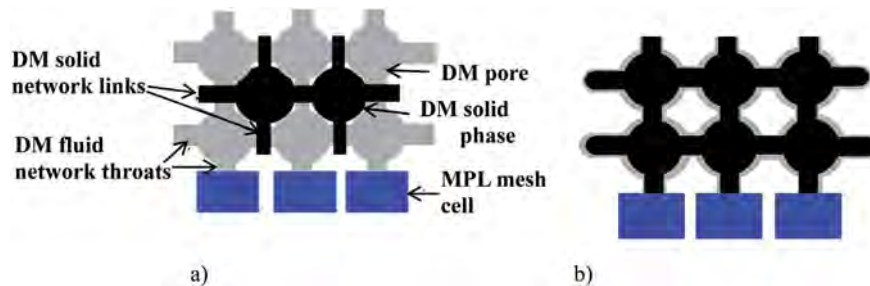

Fig. 5 — Solid and fluid networks in the DM: a) staggered solid and fluid networks, b) collocated solid and fluid networks.

conditions considered in the present paper, a standard finite volume technique on a cubic cartesian grid is used with the same spatial spacing as the lattice spacing of the DM (50 μm) in the in-plane directions and a mesh twice as finer in the through-plane direction (25 μm in mesh size) to solve the transports in the MPL. As sketched in Fig. 4, this leads to two nodes in the thickness (~50 μm) of the MPL. Each computational node of the MPL next to the DM is connected to one solid and to one fluid pore in the DM. We actually consider that the computational nodes in the MPL computational domain can be also regarded as "pores", only to test if condensation can occur in the MPL "pores" (the quotation marks are here to recall that a "realistic" pore network description of the MPL would require a much finer discretization than considered here since the pore sizes in the MPL are orders of magnitude smaller than in the DM). It turns out that condensation does not occur in the MPL "pores" in the simulations performed (see Section "Results and discussion"). Since the discretized forms of the transport equations are similar using the cubic pore network approach or a standard finite volume method, the transport phenomena in the MPL are in fact computed using the same formulations as the ones used for the DM, defining also local conductance for each of the transfer modes considered (electrical, thermal, gas diffusion, as for the DM). The MPL transport phenomena are solved with the same algorithm as for the DM (see below).

As for the DM, the different values of the conductances specified from experimental results are given in the Appendix.

As sketched in Fig. 5, each node of the MPL is connected to the corresponding throat/solid link of the GDL, for fluid and solid transfers. As the MPL and DM transport problems are discretized together over a single computational domain, the continuity of variables and fluxes at the DM/MPL interface is automatically satisfied.

Catalyst layer and membrane

A discrete representation of the catalyst layer and the membrane is used, using the same number of cells as the number of in-plane pores in the DM. Thus both layers are modeled as a collection of 52 × 52 in-plane cells connected to neighbor cells only in the through plane direction. Thus with only one node in the thickness (Fig. 4) and no in-plane transfers (on the ground that the thickness of these layers is very small compared to their in-plane extent). As a first step, this assumption is considered as sufficient as the primary aim of the model is a fine description of the DM even if coarse meshes are used for the other layers.

Each node of the CCL is connected to a fluid and to a solid node of the MPL, assuming the continuity of local gas concentrations, temperature and current density.

Oxygen flux through the membrane (to reflect oxygen permeation) is an input of the model (set to zero in the simulations presented in this work).

Coupling GDL with CCL and membrane

A key novel aspect compared to the model presented in Ref. [15] is the coupling with the CCL. To solve the above transport problems in the GDL, the distribution of j_{H_2OC}, j_{O_2C}, q_C and ψ_C must be specified over the 52 × 52 cells of the CCL, which actually form the GDL/CCL interface. These 2D fields are not known a priori but are determined as the results of the coupling between the transport phenomena and liquid formation, if any, in the GDL and the electro-chemical phenomena occurring in the CCL. With the Oxygen Reduction Reaction (ORR) $\frac{1}{2}O_2 + 2H^+ + 2e^- \rightarrow H_2O$ as the baseline for the cathode electrochemical behavior, the ORR oxygen consumption flux j_{O_2C} (mol s^{-1} m^{-2}), water production flux j_{H_2OC} (mol s^{-1} m^{-2}), and heat generation q_C (W m^{-3}) are computed as a function of the current density distribution i_C (x, y, 0) within the CCL as

$$j_{O_2C} = \frac{i_C}{4F} \tag{25}$$

$$j_{H_2OC} = -\frac{i_C}{2F} \tag{26}$$

$$q_C = \left(\frac{\Delta H}{nF} - \psi_C\right)i_C \tag{27}$$

where F is the Faraday constant (96,485 A mol^{-1}), ΔH is the ORR enthalpy (-242 kJ mol^{-1}, [32]), n is equal to 2 considering the ORR as a two-electron reaction.

The Butler−Volmer equation [33−35], written for the ORR at the cathode side, gives the relationship between the local current production rate at the CCL i_C (A cm^{-2} of catalyst) and the local overpotential at the cathode η_C (V):

$$i_C = i_{0c}\left(\exp\left(\frac{\alpha nF}{RT}\eta_C\right) - \exp\left(-\frac{(1-\alpha)nF}{RT}\eta_C\right)\right) \tag{28}$$

where R is the ideal gas constant (8.3 J mol^{-1} K^{-1}), The exchange current density i_{0c} (A cm^{-2}) in Eq. (28) is expressed as:

$$i_{0c} = n\,k_0\,\exp\left(-\frac{A_0}{RT}\right)\left(a_{O_2}^{\gamma_{O_2}}\right)^{1-\alpha}\left(a_{H_2O}^{\gamma_{H_2O}}\right)^{\alpha} \tag{29}$$

where a_{H_2O}, a_{O_2} a_{H_2} are the activities of water vapor, oxygen, and hydrogen respectively ($a_{H_2O} = \frac{P_{H_2O}}{P_{sat}}$, $a_{O_2} = \frac{P_{O_2}}{P_{ref}}$, $a_{H_2} = \frac{P_{H_2}}{P_{ref}}$ where P_{H_2O}, P_{O_2}, P_{H2} are the partial pressures of each gas, P_{sat} is the saturation vapor pressure at temperature T, P_{ref} is a reference pressure set at 1 bar).

The different parameters of the Butler−Volmer equation allow representing the behavior of the catalyst layer as a function of temperature, gas activities and over-potential. They are dependent of the properties of the catalyst layer, for instance the catalyst, carbon, and ionomer grades used, as well as the process applied to produce such catalyst layer. For the present study, the parameters are fitted on results from internal experiments [36] on given electrodes. This fitting leads to the values of k_0 (4.2 × 10^{-8} m s^{-1}), α (0.6), γ_{O2} (0.41), and γ_{H2O} (2.04). The positive sign of γ_{H2O} can be surprising as generally it is negative stating that i increases as a_{H2O} decreases. This positive value of γ_{H2O} is explained by the fact that the catalyst layer description in the model presented here does not contain explicitly the protonic transfers which increases as a_{H2O} increases. The positive value found by fitting to experimental data allows taking into account this aspect and is consistent with the experimental increase of performance of the active layer with the relative humidity (RH).

The over-potential η_C in Eq. (28) is related to the electrical potential ψ_C by

$$\psi_C = E_{rev} + \eta_C + \phi_c \tag{30}$$

where E_{rev} is the thermodynamical reversible potential (V) and ϕ_c is the protonic potential (V). The Nernst equation [37] is used for the computation of the thermodynamical reversible potential:

$$E_{rev} = \frac{\Delta H - T\Delta S}{nF} + \frac{RT}{nF}\ln\left(a_{O_2}^{\frac{1}{2}} a_{H_2} a_{H_2O}^{-1}\right) \tag{31}$$

where ΔS is the ORR entropy ($-44\ \text{J mol}^{-1}$, [32]).

The protonic potential ϕ_c (V) at the interface between the CCL and the membrane is a function of the current density through the membrane and expressed as

$$\phi_c = \phi_a + R_m\ i_C \tag{32}$$

where ϕ_a is the protonic potential along the membrane on the anode side, taken equal to zero for simplicity. This protonic potential at the anode side could be calculated (and no more used as an input parameter) with an anode electrochemical model, which could be a future extension of the current work. R_m is the resistance of the membrane expressed as $R_m = h_m/\sigma_m$ where h_m is the membrane thickness and σ_m (S m^{-1}) is the protonic resistance of the membrane; σ_m is modeled as a function of its water content λ and its local temperature [38] as,

$$\sigma_m = (33.75\lambda - 21.41)\exp\left(-\frac{1268}{T}\right) \tag{33}$$

where λ is the number of water molecules per sulfonic group [38].

$$\lambda = 0.043 + 17.81a_{H_2O} - 39.85a_{H_2O}^2 + 36a_{H_2O}^3 \tag{34}$$

The Butler−Volmer equation (Eq. (28)) varies monotonously with η. We can thus define the inverse Butler−Volmer function as the function giving η_c knowing i_C. The Butler−Volmer inverse function is denoted by $g(i_C)$. Thus

$$\eta = g(i_C) \tag{35}$$

Thus, Eq. (31) can be expressed as

$$\psi_C = E_{rev} + g(i_C) + R_m\ i_C \tag{36}$$

where, except for the very first iteration (see below), i_C is computed from the relationships

$$i_C = i = -\sigma_{MPL}\nabla\psi_c \cdot \mathbf{n} \tag{37}$$

where $\mathbf{n}$ is the unit normal vector at the CCL/MPL interface.

The simulations aim at calculating the global electrical potential together with the distributions of electrical and protonic potentials, current density, O_2, H_2O (vapor and liquid, if any), and T, as a function of the global current density for specified boundary conditions.

For each physical problem (mass, thermal and electrical transports) the mathematical system to be solved is of the form $A(X)X = B(X)$ where X contains the corresponding unknowns (temperature, gas concentrations, electrical potential, current density in the GDL...), B(X) takes into account the boundary conditions (temperature and gas concentration in the channel, current density on the rib...) and A(X) is a matrix whose coefficients notably depend on the conductances. The system is non-linear as for instance kinetic coefficients are function of gas concentration, themselves function of gas flux, and themselves function of current density. For this reason, an iterative method is necessary. This holds for the dry condition (no liquid in the assembly) as well as for the more involved wet condition (existence of liquid water in the DM).

Dry condition

The algorithm for the dry conditions is summarized in Fig. 6. To start the iteration process, the current density i^0 and the electrical potential ψ at the MPL/CCL interface are initialized imposing $i^0 = I/S_{uc}$ (S_{uc} is the in plane surface area of the cathode unit cell) and ψ from the polarization curve $U(i)$ (which is an input data) for the considered value of I. The heat flux produced by the ORR for the very first iteration is then calculated from the equation $q^0 = i^0(1.18 - U(i))$ whereas the
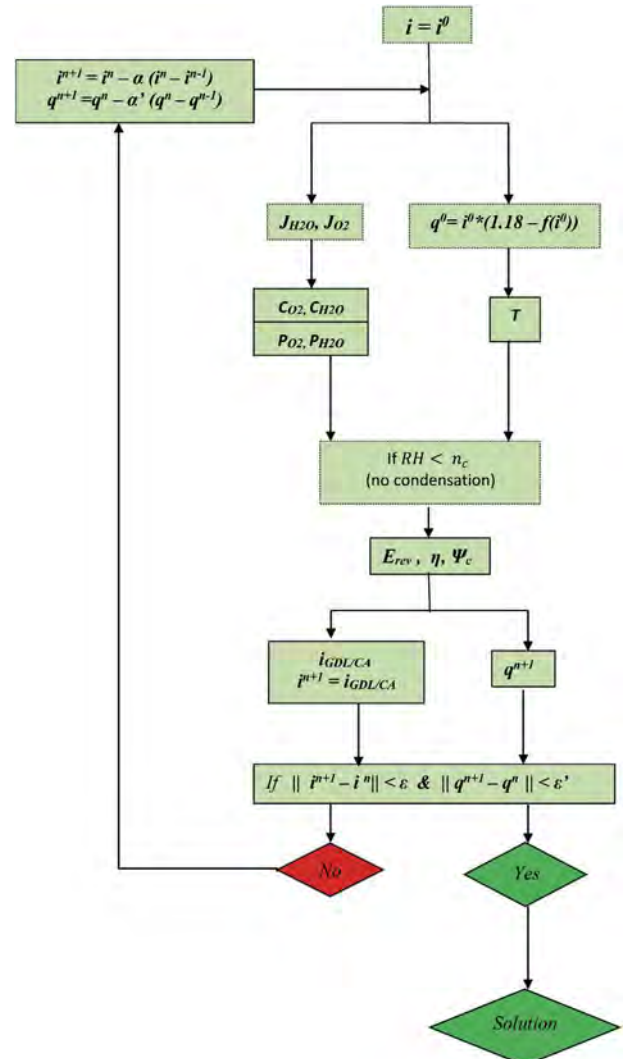

Fig. 6 − **Coupling algorithm for the dry condition.**

oxygen and water vapor fluxes at this interface are computed from Eqs. (11) and (12) combined with Eqs. (25) and (26). This gives the boundary condition to be applied for the computation of the thermal, gas and electrical transfers inside the GDL. The latter gives the gas concentrations, temperature and electrical potential in the GDL, and especially at the MPL/CCL interface. This allows updating the current density and heat flux distributions at this interface. These distributions are then used as inputs for the following iteration. The current density is no more uniform due to the presence of the channels and rib which affects the homogeneity of the transfers. The process is repeated until convergence on current density i and heat flux q is reached over the MPL/CCL interface. As indicated in Fig. 6, convergence is considered to be reached when the Euclidean norm of the variations of i and q between two successive iterations is lower than some specified small parameters ε and ε' (taken equal to 10^{-3} and 10^{-2} respectively in the simulations discussed in the next section).

As also indicated in Fig. 6, it is useful to introduce under relaxation parameters, denoted by α and α' in Fig. 6, to speed up or stabilize the numerical procedure.

Wet condition

The modeling of liquid water formation and growth in the DM is a two-steps approach similar to the one described in Ref. [15]: i) nucleation points, i.e. points where liquid water forms as a result of condensation, are identified, ii) the growth of the liquid clusters from the nucleation points is computed as a function of local conditions and local capillary forces, assuming that the growth is driven by capillary forces. Note that liquid water forming in the DM cannot flow from the DM into the MPL as the capillary entry pressure inside the MPL is much higher than the one inside the DM.

The specific treatment performed to account for condensation can be summarized as follows. To identify if condensation occurs, a nucleation parameter n_c is defined. In the simulations presented in the next section, this parameter is set to 1 (a value greater than 1 would reflect a possible supersaturation effect in the pore). Then after each iteration, the relative humidity field ($RH = \frac{P_{H_2O}}{P_{sat}}$) is computed in each pore of the DM (and the MPL) and compared to n_c. The dry condition corresponds to a situation where $RH < n_c$ in every pore after each iteration until convergence. When this is not the case, the algorithm for wet condition is used.

Once the condition $RH \geq n_c$ is reached, this means that there is condensation in at least one pore of the GDL. As a result of condensation, liquid clusters can form and grow within the GDL. Liquid water formation occurs in addition to the other transfers (gas, thermal and electrical) and induces additional coupling as the local liquid saturation reduces the local gas diffusion and then can influence the gas concentration in the CCL and thus the local current produced. This means that the computation of the liquid pattern must be performed at each step of the iterative algorithm. This computation is performed keeping constant the other unknowns. This introduces an additional step compared to the dry algorithm.

Starting from the nucleation points, the liquid cluster growth is computed using the classical invasion percolation

(IP) algorithm [39,40] combined with the computation of the net mass flow rate $\sum_{neighboring\ pores} J_{H_2O}$ at the boundary of each cluster. Note that the sizes of the throats in the through plane direction are multiplied by a factor 2 when applying the IP algorithm so as take into account the impact of the DM anisotropy on the liquid invasion. When $\sum_{neighboring\ pores} J_{H_2O} > 0$ the condensation rate at the surface of the cluster is greater than the evaporation rate from this cluster and the cluster can grow according to IP rules. Otherwise the cluster is considered as having reached an equilibrium between condensation and evaporation and cannot grow any more.

The simulation stops once each cluster has reached a steady state (condensation−evaporation equilibrium). Note that new nucleation points, if any, are detected after each growth step.

The convergence criterion is not different than for the dry conditions and is based on the convergence of the spatial distributions of current density and heat flux over the MPL/CCL interface.

The algorithm for the wet condition with liquid water forming as a result of condensation is summarized in Fig. 7.

The whole software is written in C++. This is an in-house code not using any commercial software or pieces of commercial software.

Results and discussion

To discuss the impact of the coupling between the transport phenomena in the various layers, which is a key new feature compared to the model presented in Ref. [15], solutions obtained using the coupling procedure are compared with solutions obtained without using the coupling procedure. The results presented below highlight when the coupling is expected to have a significant influence on the results, and, on the contrary, when it can be expected to have a small influence. Comparisons will be based on various transverse profiles. Those profiles are determined at the MPL/CCL interface in the median x, z plane located in the middle of the cathode unit cell (see Fig. 3 where this plane is shown).

In order to evaluate the interest of such coupling, simulations are performed for the dry as well as for the wet conditions, meaning without and with liquid water formation inside the GDL.

The non-coupled model used here is exactly the same as the coupled model described in the previous sections as regards the GDL and the boundary conditions at the GDL/rib, GDL/channel interfaces and lateral surfaces. The difference between the two models is that the catalyst layer model is not used in the non-coupled model. As the result, the current density distribution at the MPL/CCL interface is not computed anymore but given as an input. With this boundary condition, the other physical variables at the MPL/CCL interface are computed as for the coupled model. The same algorithms (Figs. 6 and 7), are actually applied in both cases. However, only one iteration is performed for the non-coupled model (to compute the various transport phenomena in the GDL for the given current density at the MPL/CCL interface) whereas the simulations are performed up to convergence for the coupled
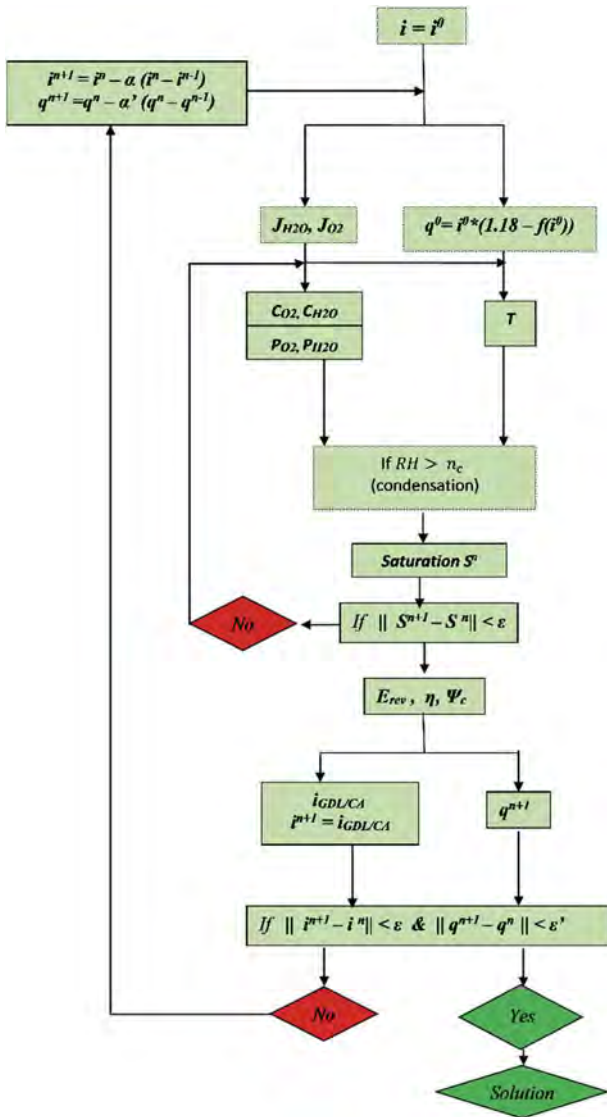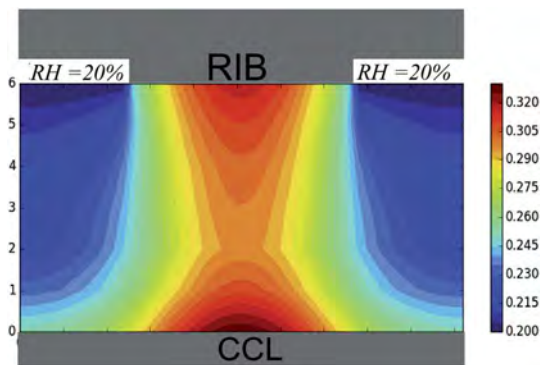
Fig. 7 − Algorithm for the wet condition.

Fig. 8 − Relative humidity distribution in a through-plane slice in the GDL (coupled model, $i = 0.6$ A cm^{-2}, $RH_{channel} = 20\%$, dry condition, $T_{rib} = 80$ °C, $\Delta T = 2$ °C, $P_{O2} = 0.21$ bar). The vertical scale is dilated for clarity.
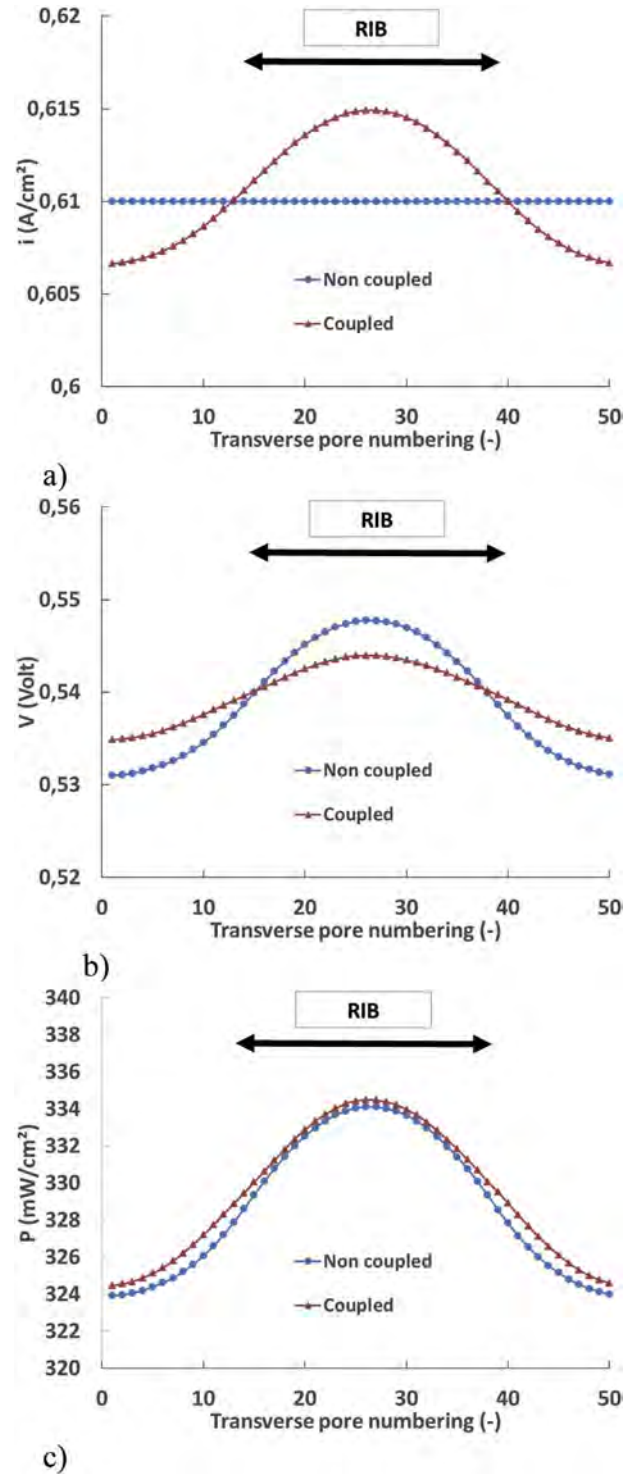

a)

b)

c)

Fig. 9 − Distribution of the current density (a), electrical potential (b), and power density (c) at the MPL/CCL interface under dry condition, $i = 0.6$ A cm^{-2}, $RH_{channel} = 20\%$, $T_{rib} = 80$ °C, $\Delta T = 2$ °C, $P_{O2} = 0.21$ bar. Results obtained with the coupled model (red curves) are compared to the results obtained with the non-coupled model (blue curves). The transverse pore numbering corresponds to the position of the 52 pores in the DM network along the rib/channel direction in the median xz plane. (For interpretation of the references to colour in this figure legend, the reader is referred to the web version of this article.)

model (so as to also determine the current density distribution at MPL/CCL interface).

All the simulations presented and discussed below are performed for temperature T_{rib} = 80 °C and gas pressure = 1.5 bar. The oxygen concentration imposed in the channel in all simulations corresponds to P_{O2} = 0.21 bar.

Dry condition

Dry conditions are typically obtained when the current density and or the relative humidity in the channel are sufficiently low. As illustrated in Fig. 8, this is for example the case in our simulations, when the relative humidity RH in the channel is equal to 20% and the average current density is i = 0.6 A cm^{-2}. Although the local relative humidity is everywhere lower than 1 in this example, it can be seen from Fig. 8 that the relative humidity is higher in the central region of the GDL below the rib. This prefigures the most likely place of condensation when RH and/or i will be increased (see below the "Wet condition" section).

The corresponding current density profile at the MPL/CCL interface computed with the coupled model is depicted in Fig. 9a. This profile is smooth and characterized by a slight maximum below the rib. This indicates that the limiting factor for performance is most probably due to electrical transfers inside the GDL rather than to gas species diffusion transfers.

As can be seen from Fig. 9, the local current density and the electrical potential distributions at the MPL/CCL interface for this case are nearly the same between the non-coupled and the coupled models. This suggests that the coupling between GDL and CCL is not a first order issue when considering the computation of the transfers at the cathode, at least when the current density and relative humidity in the channel are sufficiently low. This is confirmed by the power density profiles shown in Fig. 9c. The average power density is 328.7 mW cm^{-2} with the non-coupled model and 329.3 mW cm^{-2} with the coupled model. This is consistent with the fact that in both cases the current density profiles are nearly the same, so are the heat fluxes, gas concentrations, and electrical potentials.

As can be seen from Fig. 10, increasing the mean current density from 0.6 A cm^{-2} to 1.4 A cm^{-2} in order to enhance the differences between the two models first leads to higher values of the local relative humidity than at i = 0.6 A cm^{-2} (maximum is 0.45 instead of 0.33) but still lower than 100% everywhere in
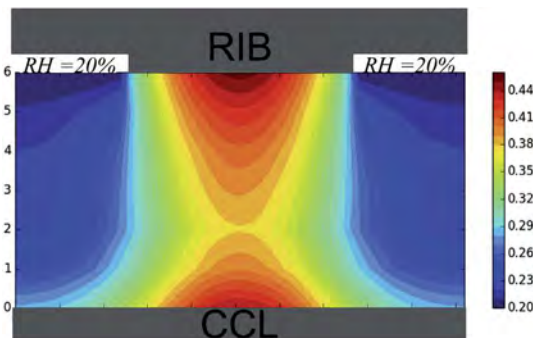

Fig. 10 — Relative humidity distribution in a through-plane slice in the GDL (coupled model, i = 1.4 A cm^{-2}, $RH_{channel}$ = 20%, T_{rib} = 80 °C, ΔT = 2 °C, P_{O2} = 0.21 bar, dry condition). The vertical scale is dilated for clarity.
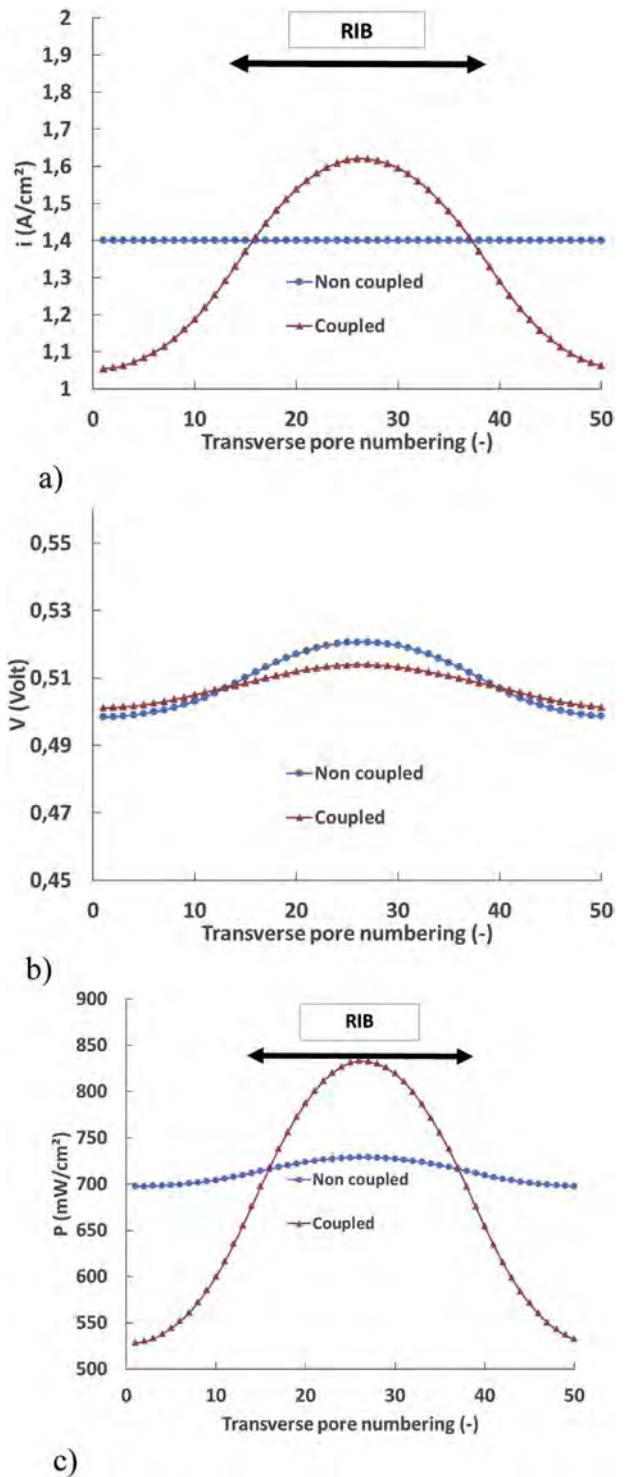

a)

b)

c)

Fig. 11 — Distribution of the current density (a), electrical potential (b), and power density (c) at the MPL/CCL interface under dry condition, i = 1.4 A cm^{-2}, $RH_{channel}$ = 20%, T_{rib} = 80 °C, ΔT = 2 °C, P_{O2} = 0.21 bar. Results obtained with the coupled model (red curves) are compared to the results obtained with the non-coupled model (blue curves). The transverse pore numbering corresponds to the position of the 52 pores in the DM network along the rib/channel direction in the median xz plane. (For interpretation of the references to colour in this figure legend, the reader is referred to the web version of this article.)
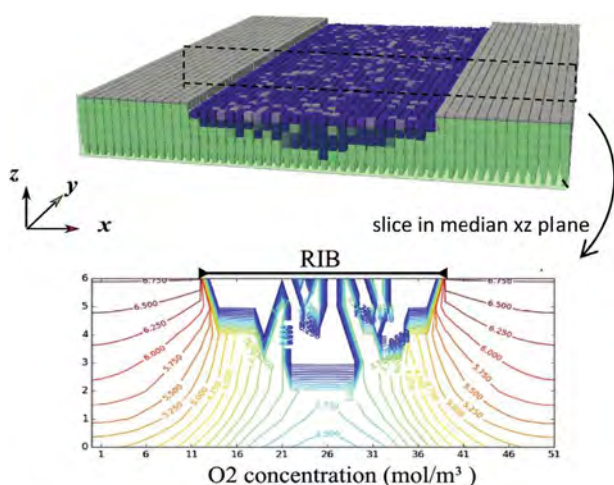
the GDL. The comparison between Figs. 8 and 10 show that the local relative humidity is again higher in the central region below the rib but it seems that the maximum is now right below the rib (Fig. 10) rather than at the MPL/CCL interface (Fig. 8). As shown in Fig. 11a, the current density profile computed with the coupled model is still smooth with again a maximum below the rib. So the limiting factor is suspected to be also the electrical transfers. As depicted in Fig. 11b, the electrical potential profile is not so different between the two models but the current density and the power density profiles are modified. The average power density is 712 mW cm^{-2} with the non-coupled model against 673 cm^{-2} with the coupled model (so roughly 5% lower), showing that the increase of the average current density increases the non-uniformities within the MEA. Thus, the coupling between the GDL and the CCL appears to be more and more important and necessary as the average current density is increased.

Wet condition

As can be seen from Fig. 12, a significant fraction of the DM pore space is invaded by liquid water as a result of condensation when the relative humidity is set equal to 90% in the channel and the average current density set equal to 1.4 A cm^{-2}.

As can be seen from Fig. 13, the current density profile then changes significantly. A significant minimum appears below the rib, meaning that the dominant limiting factor for performance is not the electrical transfer in the GDL anymore as for the dry case, but the diffusion transfer of the gaseous species. This can be attributed to the presence of liquid water appearing below the rib. This liquid region reduces the region below the rib available for the oxygen transport and thus reduces the oxygen diffusion through the GDL (as illustrated in Fig. 12).

As shown in Fig. 13, the local current density, the electrical potential, and the electrical power density profiles at the MPL/CCL interface are completely different between the coupled
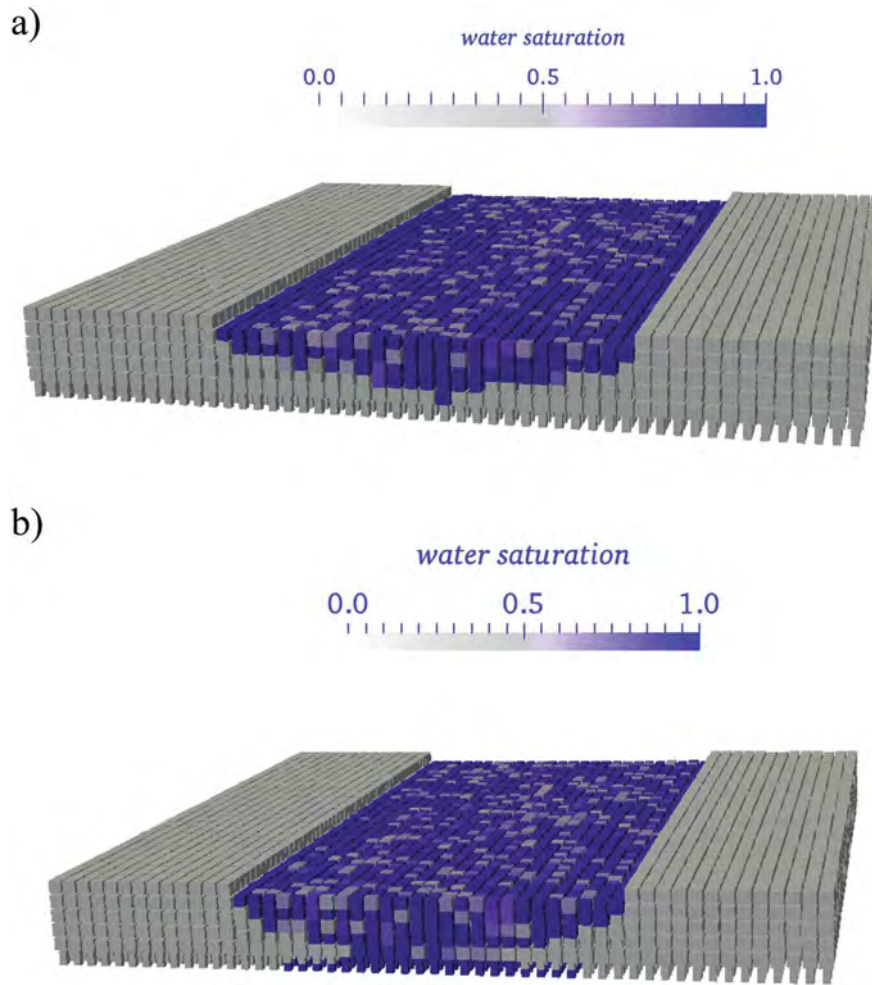
and the non-coupled models for this wet condition. As illustrated in Fig. 14, this is mainly due to the fact that the liquid water distribution is different in both cases with a greater amount of liquid water close to the CCL with the non-coupled model. This can be explained by the fact that in the non-

a)

b)

c)
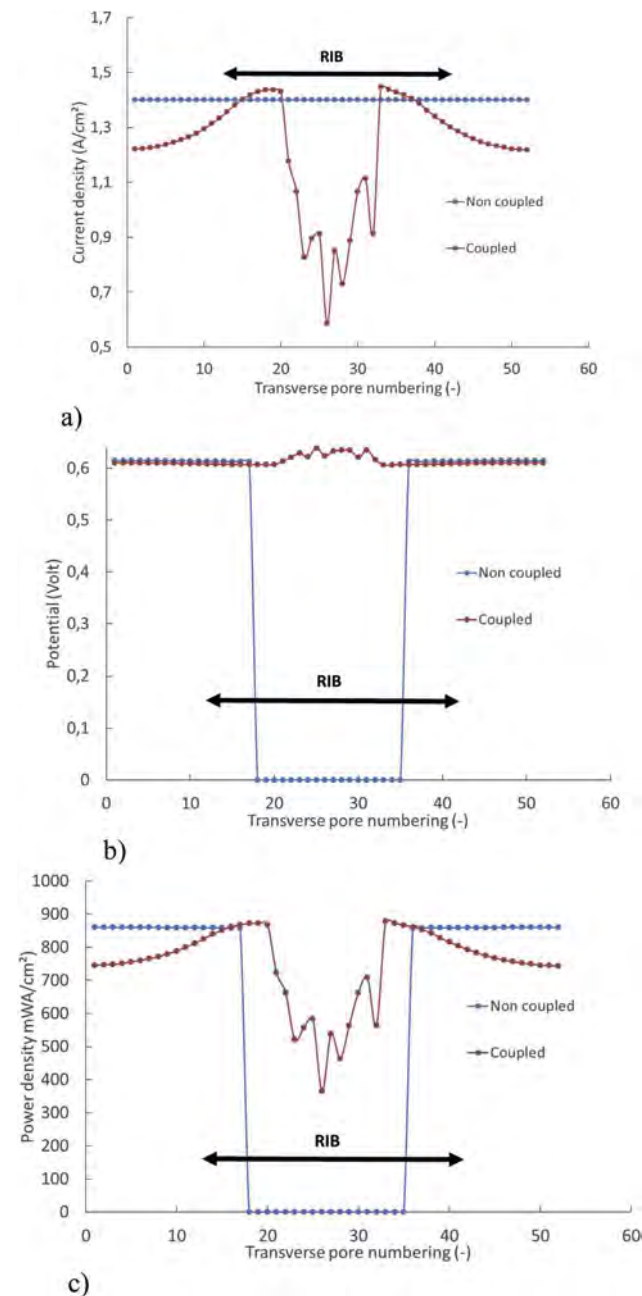
Fig. 13 — Distribution of the current density (a), electrical potential (b), and power density (c) at the MPL/CCL interface under wet condition, i = 1.4 A cm^{-2}, RH$_{channel}$ = 90%, T$_{rib}$ = 80 °C, ΔT = 2 °C, P$_{O2}$ = 0.21 bar. Results obtained with the coupled model (red curves) are compared to the results obtained with the non-coupled model (blue curves). The transverse pore numbering corresponds to the position of the 52 pores in the DM network along the rib/channel direction in the median xz plane. (For interpretation of the references to colour in this figure legend, the reader is referred to the web version of this article.)

Fig. 12 — Impact of liquid water (in blue) produced by condensation on oxygen diffusion distribution in GDL (coupled model, wet condition, i = 1.4 A cm^{-2}, RH$_{channel}$ = 90% T$_{rib}$ = 80 °C, ΔT = 2 °C, P$_{O2}$ = 0.21 bar). (For interpretation of the references to colour in this figure legend, the reader is referred to the web version of this article.)

Fig. 14 — Liquid water (in blue) distribution in the DM under wet condition for the coupled (a) and non-coupled (b) models; $i = 1.4$ A cm^{-2}, RH$_{channel} = 90\%$, $T_{rib} = 80$ °C, $\varDelta T = 2$ °C, $P_{O2} = 0.21$ bar. (For interpretation of the references to colour in this figure legend, the reader is referred to the web version of this article.)

coupled model, the current density profile at the MPL/CCL interface is uniform and thus the heat flux is also uniform, whereas the current density and heat flux are strongly non-uniform with the coupled model and significantly lower below the rib than in the non-coupled case. As a result, the vapor flux injected in the region below the rib is much greater with non-coupled model since this flux is directly proportional to the current density (Eq. (26)). The power density profiles are also different in both cases, with an average power density around 561 mW cm^{-2} with the non-coupled model and 750 mW cm^{-2} with the coupled one (so roughly + 35%). This is a strong indication that the coupling with the CCL must be taken into account in order to compute the transfers when liquid water forms inside the GDL.

Interestingly the fact the local current density inside the MEA is different between the regions located below the rib and below the channel is consistent with the experimental measurements reported in Refs. [41,42].

As exemplified in Fig. 14, the coupled model and the non-coupled models both lead to the typical liquid distribution already discussed in Ref. [15] characterized by a strong separation between the region below the rib, where the liquid water accumulates, and the region below the channel, which remains dry.

Conclusions

In this paper, a model of a PEMFC cathode is proposed, coupling the electro-chemical phenomena taking place in the catalyst layer with a Pore Network Model (PNM) for computing the transfers and the liquid water formation in the diffusion medium (DM) of a GDL and a continuum approach in the MPL. A distinguishing feature of PNM is to model the liquid water formation by condensation in the DM and to assume that the water formed in the CCL enters the GDL in vapor form. For the conditions studied, the present study indicates that liquid water formation due to condensation takes place in the region of the GDL below the rib confirming the results obtained in Ref. [15] with a non-coupled model. The results show that it is important to take into account the coupling with the CCL as the current density profile at the CCL/GDL interface is essential for simulating the performance of the MEA. This is crucial when liquid water appears in the GDL because of the impact of the liquid water formation on the gas transport.

More generally, the study illustrates that correctly predicting the liquid water pattern is very important for predicting the transfers and the performance of the MEA.

Consequently, as the two-phase patterns are fully different between the condensation scenario in the GDL considered here (strong separation effect with the liquid water located in the central region below the rib) and the more classical scenario of injection directly in liquid phase (not leading typically to the channel–rib separation effect), there is still a need to better understand the water formation in the GDL. For example, we surmise that the condensation scenario considered in the present paper is well adapted to the situations where the operating temperature is sufficiently high (~80 °C) since as mentioned in the introduction it leads to several results in good agreement with experiments for this condition. For sufficiently low operating temperatures, considering that all the produced water enters the GDL in vapor phase might be a too restrictive assumption and mixed scenario combining condensation–evaporation with liquid injection could be an interesting option. Also, we have not considered situations where the liquid water can reach the channel (the relative humidity in our simulation is always lower than 100% in the channel). This case would also deserve to be studied.

The present model needs improvements also for the conditions to which it is a priori well adapted. For instance, the discretization of the MPL must be refined as well as in the CCL with the consideration of the in-plane transport. The impact of liquid water on GDL thermal conductivity, the consideration of phase change phenomena on the thermal transport in the GDL are also to be included in the model for better descriptions. Here, the objective was more modest. It was to introduce a methodology for the coupling and to evaluate the impact of the latter.

Acknowledgements

Appendix

Transport parameters of the GDL model are fitted by comparing results from the model to available measurements on SGL 25 BA (DM only) and SGL 25BC (DM and MPL). When the desired data are not found in the literature, in-house measurements and/or results on other GDL are used. This fitting allows finding, for each physical transfer:

- the "tortuosity" coefficients β of the DM, under the rib and under the channel, in-plane (denoted with subscript //) and through-plane (denoted with subscript ⊥)
- the conductances g of the MPL considered as isotropic and not compressible

These parameters are given in the tables below with also a comparison of effective properties as modeled and as measured on the DM/MPL assembly to check the consistency of the model.

Table 1 — Coefficients used for modeling the gas transfer. (*) evaluation from Ref. [43] with $D_{bin} = 0.35$ cm² s⁻¹.

Gas diffusion		Rib		Channel	
		//	⊥	//	⊥
DM	Tortuosity β (−)	1	0.4	1	0.4
MPL	g (m³ s⁻¹)	1.9×10^{-9}	1.9×10^{-9}	1.9×10^{-9}	1.9×10^{-9}
SGL 25BC	D_{eff}/D_{bin} (Experiments)	−	−	−	~0.17 (*)
	D_{eff}/D_{bin} (Simulation)	0.5	0.08	0.6	0.15

Table 2 — Coefficients used for modeling the electrical transfer; (*) evaluation from in-house measurements, (**) [44].

Electrical transfer		Rib		Channel	
		//	⊥	//	⊥
DM	Tortuosity β (−)	1	4.2e-2	0.8	2.2e-2
MPL	g (S)	0.2	0.2	0.2	0.2
SGL 25BC	σ (S m⁻¹) (Experiments)	3412–7148 (*)	−	2815–4891 (*)	<195 (**)
	σ (S m⁻¹) (Simulation)	5500	300	4300	170

Table 3 — Coefficients used for modeling the thermal transfer; (*) Evaluation from Ref. [45]. The thermal anisotropy is evaluated by analogy with electrical anisotropy $\frac{\lambda_{T//}}{\lambda_{T\perp}} = \frac{\sigma_{e//}}{\sigma_{e\perp}}$.

Thermal transfer		Rib		Channel	
		//	⊥	//	⊥
DM	Tortuosity β (−)	0.75	0.026	0.6	0.013
MPL	g (W K⁻¹)	2	2	2	2
SGL 25BC	κ (W m⁻¹ K⁻¹) (Experiments)	−	~0.235 (*)	−	−
	κ (W m⁻¹ K⁻¹) (Simulation)	4.6	0.25	4.3	0.17

REFERENCES

[1] Yu X, Zhou B, Sobiesiak A. Water and thermal management for Ballard PEM fuel cell stack. J Power Sources 2005;147:184—95.

[2] Borup R, Meyers J, Pivovar B, Kim YS. Scientific aspects of polymer electrolyte fuel cell durability and degradation. Chem Rev 2007;107(10):3904—51.

[3] Benziger J, Nehlsen J, Blackwell D, Brennan T, Itescu J. Water flow in the gas diffusion layer of PEM fuel cells. J Membr Sci 2005;261:98—106.

[4] Dutta S, Shimpalee S, Van Zee JW. Numerical prediction of mass-exchange between cathode and anode channels in a PEM fuel cell. Int J Heat Mass Transf 2001;44:2029—42.

[5] Siegel NP, Ellis MW, Nelson DJ, von Spakovsky MR. A two-dimensional computational model of a PEMFC with liquid water transport. J Power Sources 2004;128:173—84.

[6] Meng H, Wang CY. Large-scale simulation of polymer electrolyte fuel cells by parallel computing. Chem Eng Sci 2004;59:3331—43.

[7] Rebai M, Prat M. Scale effect and two-phase flow in a thin hydrophobic porous layer. Application to water transport in gas diffusion layers of PEM fuel cells. J Power Sources 2009;192:534—43.

[8] Gostick JT, Ioannidis MA, Fowler MW, Pritzker MD. Pore network modeling of fibrous gas diffusion layers for polymer electrolyte membrane fuel cells. J Power Sources 2007;173:277—90.

[9] Pulloor Kuttanikkad S, Prat M, Pauchet J. Pore-network simulations of two-phase flow in a thin porous layer of mixed wettability: application to water transport in gas diffusion layers of proton exchange membrane fuel cells. J Power Sources 2011;196:1145—55.

[10] Pauchet J, Prat M, Schott P, Pulloor Kuttanikkad S. Performance loss of proton exchange membrane fuel cell due to hydrophobicity loss in gas diffusion layer: analysis by multiscale approach combining pore network and performance modeling. Int J Hydrogen Energy 2012;37(2):1628—41.

[11] El Hannach M, Prat M, Pauchet J. Pore network model of the cathode catalyst layer of proton exchange membrane fuel cells: analysis of water management and electrical performance. Int J Hydrogen Energy 2012;37(4):18996—9006.

[12] Belgacem N, Agaësse T, Pauchet J, Prat M. Liquid invasion from multiple inlet sources and optimal gas access in a two-layer thin porous medium. Transp Porous Media 2016;115(3):449—72.

[13] Gostick JT. Random pore network modeling of fibrous pemfc gas diffusion media using voronoi and delaunay tessellations. J Electrochem Soc 2013;160(8):F731—43.

[14] Agaësse T, Lamibrac A, Buechi F, Pauchet J, Prat M. Gostick? J Power Sources 2016;331:462—74.

[15] Straubhaar B, Pauchet J, Prat M. Pore network modelling of condensation in gas diffusion layers of proton exchange membrane fuel cells. Int J Heat Mass Transf 2016;102(1):891—901.

[16] Oberholzer P, Boillat P. Local characterization of PEFCs by differential cells: systematic variations of current and asymmetric relative humidity. J Electrochem Soc 2014;161(1):F139—52.

[17] LaManna JM, Chakraborty S, Gagliardo JJ, Mench MM. Isolation of transport mechanisms in PEFCs using high resolution neutron imaging. Int J Hydrogen Energy 2014;39:3387—96.

[18] Ceballos L, Prat M. Invasion percolation with multiple injections and the water management problem in proton exchange membrane fuel cell. J Power Sources 2010;195:825—8.

[19] Straubhaar B, Pauchet J, Prat M. Water transport in gas diffusion layers of PEM fuels cells in presence of a temperature gradient. Phase change effect. Int J Hydrogen Energy 2015;40(35):11668—75.

[20] Alink R, Gerteisen D. Modeling the liquid water transport in the gas diffusion layer for polymer electrolyte membrane fuel cells using a water path network. Energies 2013;6(9):4508—30.

[21] Alink R, Gerteisen D. Coupling of a continuum fuel cell model with a discrete liquid water percolation model. Int J Hydrogen Energy 2014;39:8457—73.

[22] Qin CZ, Hassanizadeh SM, Van Oosterhout LM. Pore-network modeling of water and vapor transport in the micro porous layer and gas diffusion layer of a polymer electrolyte fuel cell. Computation 2016;4(2):21.

[23] Zenyuk IV, Medici EF, Allen JS, Weber AZ. Coupling continuum and pore-network models for polymer-electrolyte fuel cells. Int J Hydrogen Energy 2015;40:16831—45.

[24] Medici EF, Zenyuk IV, Parkinson DY, Weber AZ, Allen JS. Understanding water transport in polymer electrolyte fuel cells using coupled continuum and pore-network models. Fuel Cells 2016;16:725—33.

[25] Aghighi M, Hoeh MA, Lehnert W, Merle G, Gostick J. Simulation of a full fuel cell membrane electrode assembly using pore network modeling. J Electrochem Soc 2016;163(5):F384—92.

[26] Stauffer D. Introduction to percolation theory. 2nd ed. CRC Press; 1994.

[27] Eller J, Rose T, Marone F, Stampanoni M, Wokaun A, Bchi FN. Progress in in situ X-ray tomographic microscopy of liquid water in gas diffusion layers of PEFC. J Electrochem Soc 2011;158(8):B963—70.

[28] http://ansatte.hin.no/ra/MatLinks/carbonfiber_overview.pdf, 20-06-2015.

[29] http://zoltek.com/carbonfiber/, 20-06-2015.

[30] Incropera FP, Dewitt DP. Fundamentals of heat and mass transfer. 5th ed. 2001.

[31] Burheim OS, Pharoah JG, Lampert H, Vie PJS, Kjelstrup S. Through-plane thermal conductivity of PEMFC porous transport layers. J Fuel Cell Sci Tech 2011;8:021013.

[32] Zhang J. PEM fuel cells electrocatalysts and catalyst layers. Springer editions, ISBN 978-1-84800-935-6.

[33] Erdey-Gruz T, Volmer M. Zur theorie der wasserstoffüberspannung. Z Phys Chem (A) 1930;150:203—13.

[34] Mann RF, Amphlett JC, Hooper MAI, Jensen HM, Peppley BA, Roberge PR. Development and application of a generalised steady-state electrochemical model for a PEM fuel cell. J Power Sources 2000;86:173—80.

[35] Mann RF, Amphlett JC, Peppley BA, Thurgood CP. Application of Butler—Volmer equations in the modelling of activation polarization for PEM fuel cells. J Power Sources 2006;161:775—81.

[36] Project Chameau, Synthèse des études de modélisation des performances; unpublished CEA internal report.

[37] Kordesch K, Simader G. Fuel Cells and their applications. 1996.

[38] Springer TE, Zawodzinski TA, Gottesfeld S. Polymer electrolyte fuel cell model. J Electrochem Soc 1991;138:2334—42.

[39] Wilkinson D, Willemsen JF. Invasion percolation: a new form of percolation theory. Phys A Math Gen 1983;16:3365—76.

[40] Chapuis O, Prat M, Quintard M, Chane-Kane E, Guillot O, Mayer NJ. Two-phase flow and evaporation in model fibrous media: application to the gas diffusion layer of PEM fuel cells. J Power Sources 2008;178:258—68.

[41] Freunberger SA, Reum M, Evert J, Wokau A, Büchi FN. Measuring the current distribution in PEFCs with sub-millimeter resolution. J Electrochem Soc 2006;153:A2158—65.

[42] Rachidi S. Développement et exploitation d'une micro-instrumentation pour les piles à combustible de type PEMFC

[unpublished Ph.D. thesis]. France: Grenoble University; 2011.

[43] LaManna JM, Kandlikar SG. Determination of effective water vapor diffusion coefficient in pemfc gas diffusion layers. Int J Hydrogen Energy 2011;36:5021—9.

[44] http://fuelcellmarkets.com/content/images/articles/GDL_24_25_Series_Gas_Diffusion_Layer.pdf, 20-06-2015.

[45] Thomas A, Maranzana G, Didierjean S, Dillet J, Lottin O. Thermal and water transfer in PEMFCs: investigating the role of the microporous layer. Int J Hydrogen Energy 2014;39:2649—58.